Supplemental material:
Full transmission and reflection of waves propagating through a maze of disorder

Benoît Gérardin, Jérôme Laurent, Arnaud Derode, Claire Prada, and Alexandre Aubry*
ESPCI ParisTech, PSL Research University, CNRS, Univ Paris Diderot,
Sorbonne Paris Cité, Institut Langevin, UMR 7587, 1 rue Jussieu, F-75005 Paris, France
(Dated: September 26, 2014)

CONSTRUCTION OF THE CHANNEL BASIS

The first part of this section describes the flexural modes supported by the homogeneous plate and the associated wavenumbers. In a second part, we describe the transformation from the point-to-point basis in which measurements are performed and the channel basis that is built from the homogeneous plate eigenmodes.

The flexural modes are derived using the thin plate approximation [1, 2] since the wavelength λ and the width W of the waveguide are much greater than its thickness d. In this limit, the out-of-plane component of the vibration, $w(x,y)$, is constant over the plate thickness. It satisfies the following equation of motion [1, 2]

$$\rho d\frac{\partial^2 w}{\partial t^2} + D\nabla_\perp^4 w = 0 \qquad \text{(S1)}$$

with $\nabla_\perp$ the horizontal gradient operator, ρ is the material density and D is the flexural rigidity which can be expressed as

$$D = \frac{Ed^3}{12(1-\nu^2)}$$

with E the Young modulus and ν the Poisson ratio. As the equation of motion (Eq. S1) is fourth order, there exists, at each pulsation ω, two sets of modes, $w^{(e)}(y)e^{ikx}$ and $w^{(o)}(y)e^{ikx}$, that are either even or odd with respect to the $y-$axis. The application of stress-free boundary conditions at $y = \pm W/2$ leads to the following expressions for these modes [2]

$$w^{(e)}(y) = A\left[\cosh\left(\frac{\chi_m W}{2}\right)\cosh\left(\chi_p y\right) - \frac{k^2\nu-\chi_p^2}{k^2\nu-\chi_m^2}\cosh\left(\frac{\chi_m W}{2}\right)\cosh\left(\chi_m y\right)\right] \qquad \text{(S2)}$$

$$w^{(o)}(y) = A\left[\sinh\left(\frac{\chi_m W}{2}\right)\sinh\left(\chi_p y\right) - \frac{k^2\nu-\chi_p^2}{k^2\nu-\chi_m^2}\sinh\left(\frac{\chi_m W}{2}\right)\sinh\left(\chi_m y\right)\right] \qquad \text{(S3)}$$

where $\chi_p = \sqrt{k^2+K^2}$, $\chi_m = \sqrt{k^2-K^2}$, $K^2 = \omega\sqrt{\rho d/D}$ and A a normalization constant such that $\int_{-W/2}^{W/2} dy \left|w^{(o,e)}(y)\right|^2 = 1$. The dispersion relations $\omega(k)$ can be derived by solving the following transcendental equations [1]

$$\left[K^2+(1-\nu^2)k^2\right]\chi_m \tanh\left(\chi_m W/2\right) = \left[K^2-(1-\nu^2)k^2\right]\chi_p \tanh\left(\chi_p W/2\right), \qquad \text{(S4)}$$

for even modes, and

$$\left[K^2+(1-\nu^2)k^2\right]\chi_m \coth\left(\chi_m W/2\right) = \left[K^2-(1-\nu^2)k^2\right]\chi_p \coth\left(\chi_p W/2\right) \qquad \text{(S5)}$$

for odd modes. It yields the wavenumber $k_i^{(o,e)}$ associated to each mode $w_i^{(o,e)}$ at a pulsation ω.

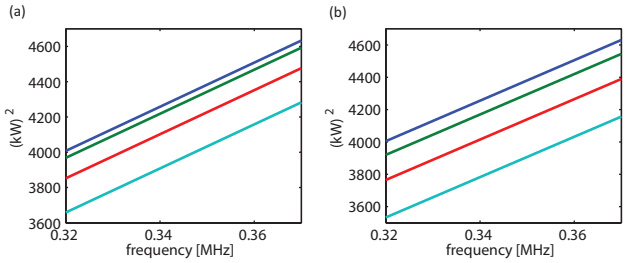

FIG. S1: Dispersion curves of the first four flexural modes for even (a) and odd (b) components. The wavenumber k is scaled by the width W.

Fig. S1 displays the dispersion curves obtained for even and odd modes in our experimental conditions. The $y-$dependence of the first four even and odd eigenmodes at $f = 0.36$ MHz are shown in Fig. S2. Note that, unlike a classical wave-guide, the flexural modes of an elastic plate are not simple sinusoids but display evanescent components due to edge effects at the boundaries of the plate.

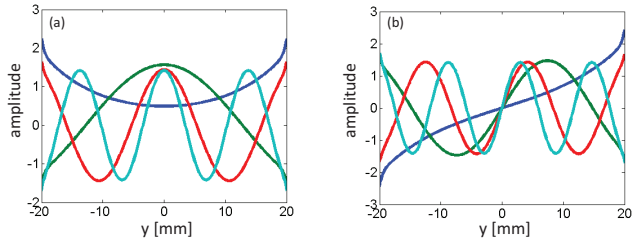

FIG. S2: $y-$dependence of the first four even (a) and odd (b) flexural eigenmodes at $f = 0.36$ MHz.

Cross and Lifshiftz [1] also derived the flux ϕ carried by the flexural modes through an homogeneous thin plate

$$\phi = kWI(\nu) \qquad \text{(S6)}$$

where $I(\nu)$ a constant that solely depends on the Poisson ratio ν. ϕ is directly proportional to the wavenumber k. Hence, one can force each mode $w_i^{(o,e)}$ to carry the same energy

flux by renormalizing each mode by the square root of its wavenumber $k_i^{(o,e)}$.

Now that the eigenmodes of the plate have been derived, one can define the transformation matrix $\mathbf{p}$ from the point-to-point basis to the channel basis. $\mathbf{p}$ is of dimension $N \times M$. Its elements correspond to the values of the N eigenmodes taken at the M positions y_i where the field is measured. Each mode is normalized by the square root of its wavenumber such that each of them carries the same energy flux. $\mathbf{p}$ is thus given by

$$\mathbf{p} = \begin{bmatrix} \frac{w_1^{(o)}(y_1)}{\sqrt{k_1^{(o)}}} & \cdots & \frac{w_1^{(o)}(y_M)}{\sqrt{k_1^{(o)}}} \\ \vdots & & \vdots \\ \frac{w_{N/2}^{(o)}(y_1)}{\sqrt{k_{N/2}^{(o)}}} & \cdots & \frac{w_{N/2}^{(o)}(y_M)}{\sqrt{k_{N/2}^{(o)}}} \\ \frac{w_1^{(e)}(y_1)}{\sqrt{k_1^{(e)}}} & \cdots & \frac{w_1^{(e)}(y_M)}{\sqrt{k_1^{(e)}}} \\ \vdots & & \vdots \\ \frac{w_{N/2}^{(e)}(y_1)}{\sqrt{k_{N/2}^{(e)}}} & \cdots & \frac{w_{N/2}^{(e)}(y_M)}{\sqrt{k_{N/2}^{(e)}}} \end{bmatrix} \tag{S7}$$

From the reflection/transmission matrices measured in the point-to-point basis ($\mathbf{r_p}$, $\mathbf{t_p}$, $\mathbf{r'_p}$, $\mathbf{t'_p}$), one can deduce the reflection/transmission matrices in the channel basis ($\mathbf{r_c}$, $\mathbf{t_c}$, $\mathbf{r'_c}$, $\mathbf{t'_c}$) through the following matrix product

$$\mathbf{r_c} = \mathbf{p} \times \mathbf{r_p} \times \mathbf{p}^T \tag{S8}$$
$$\mathbf{r'_c} = \mathbf{p} \times \mathbf{r'_p} \times \mathbf{p}^T \tag{S9}$$
$$\mathbf{t_c} = \mathbf{p} \times \mathbf{t_p} \times \mathbf{p}^T \tag{S10}$$
$$\mathbf{t'_c} = \mathbf{p} \times \mathbf{t'_p} \times \mathbf{p}^T \tag{S11}$$

The $\mathbf{S}$-matrix can be finally deduced in the properly defined channel basis,

$$\mathbf{S} = \begin{pmatrix} \mathbf{r_c} & \mathbf{t'_c} \\ \mathbf{t_c} & \mathbf{r'_c} \end{pmatrix} \tag{S12}$$

ORIGINS AND MAGNITUDE OF THE EXPERIMENTAL NOISE

In this section, we first derive the magnitude of noise in the experiment and then account for its various origins and its nature.

The SNR in our measurements has been estimated as follows. In theory, reciprocity implies the strict equalities $r_{ij} = r_{ji}$ and $r'_{ij} = r'_{ji}$ for all the elements of the reflection matrices and the equality $t_{ij} = t'_{ji}$ for all the elements of transmission matrices. Due to noise, these equalities are not strictly checked and, by comparing the *supposed* reciprocal elements, one can estimate the SNR in the measurements:

$$SNR = -\frac{1}{4}\left[10\log_{10}\times\left(\frac{\left\langle |r_{ij}-r_{ji}|^2\right\rangle_{\{(i,j)|i\neq j\}}}{\left\langle |r_{ij}|^2\right\rangle_{\{(i,j)|i\neq j\}}}\right) + 10\log_{10}\times\left(\frac{\left\langle |r'_{ij}-r'_{ji}|^2\right\rangle_{\{(i,j)|i\neq j\}}}{\left\langle |r'_{ij}|^2\right\rangle_{\{(i,j)|i\neq j\}}}\right) + 2\times 10\log_{10}\left(\frac{\left\langle |t_{ij}-t'_{ji}|^2\right\rangle_{\{(i,j)\}}}{\left\langle |t_{ij}|^2\right\rangle_{\{(i,j)\}}}\right)\right]$$

where the symbol $\langle\cdots\rangle$ denotes an average over the indices in the subscript. Following this method, the experimental SNR has been estimated at 8.5 dB, that is to say we have to deal with noise fluctuations of 14% in intensity.

We now investigate the various origins of noise in our experiment. Fig. S3(a) displays a set of 100 impulse responses for the same source/receiver position. Each signal is averaged over 128 laser shots as for the measurement of the $\mathbf{S}$-matrix. We have chosen to reproduce 100 times the experiment because each point is used 100 times as a source in the measurement of the $\mathbf{S}$-matrix. Hence, we are exactly in the same conditions. In Fig. S3(a), the first part of the signals (from -50 μs to -10 μs) corresponds to electronic additive noise. The second part (from -10 μs to +10 μs) corresponds to the source signals. A zoom on this part of the signals is plotted in Fig. S3(b). At last, the third part (from +10 μs to +120 μs) corresponds to the signals reflected by the disordered slab.

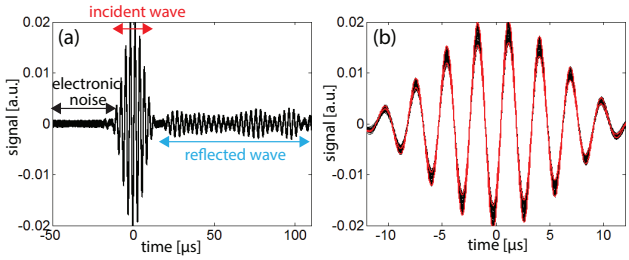

FIG. S3: (a) Set of 100 impulse responses measured in the case of an excitation and a detection at the same point. The signals have been filtered over the 0.3-0.4 MHz bandwidth (b) Zoom on the emission signals highlighting the fluctuations of the thermo-elastic conversion efficiency.

• The first source of noise comes from the laser-induced deformation of the plate surface. To obtain a satisfying signal-to-noise ratio, we actually work close to the ablation threshold [3]. The slight change of the surface state after each laser shot leads to fluctuations in the thermo-elastic conversion efficiency [see Fig. S3(b)]. It manifests itself as a multiplicative noise of 1% in intensity.

• The second source of noise comes from long-term laser power fluctuations. These fluctuations have been measured with a power meter and account for a multiplicative noise of 1.5% in intensity over the time of the experiment (20 hours).

• The third source of noise is the electronic additive noise diplayed by Fig. S3(a). It accounts for an additive noise of 5%

in reflection and 10% in transmission since the transmitted intensity is about two times smaller than the reflected one in our experiment. One can say that we could have reduced this additive noise by more averaging. However, it would have implied more laser shots at each source point, hence more fluctuations in the thermo-elastic conversion efficiency. Thus, we had to make the best compromise between this electronic additive noise and the multiplicative noise due to surface damaging.

• At last, the remaining source of noise comes from a miscalibration of the heterodyne interferometer at few points of measurements (4 points over 100): the specular reflection of light on the plate can be deteriorated by its roughness and by a slight bending near its edges induced by the cutting tool. This calibration issue manifests itself as a multiplicative noise (4% in intensity) in the $\mathbf{S}-$matrix once projected in the channel basis.

NORMALIZATION OF S: HOW TO RETRIEVE THE OPEN CHANNELS IN PRESENCE OF NOISE?

In this section, we show, by means of a simple numerical simulation, how the normalization of $\mathbf{S}$ performed in the accompanying Letter allows to retrieve the open channels in presence of both multiplicative and additive noise.

We have numerically generated 1000 realizations of a unitary symmetric random matrix $\mathbf{S_o}$ of dimension $2N \times 2N$ with a conductance similar to the one measured experimentally ($g \sim 8$). As expected, the mean distribution of the transmission eigenvalues T_o (not shown here) follows the bimodal law (Eq.3 of the accompanying Letter). Then, experimental noise is simulated by generating two random matrices $\mathbf{N}$ and $\mathbf{N'}$. $\mathbf{N}$ accounts for multiplicative noise: its elements are real gaussian random variables with zero mean. $\mathbf{N'}$ accounts for additive noise: its elements are circularly symmetric complex gaussian random variables with zero mean. A *noisy* scattering matrix $\mathbf{S}$ is then obtained, such that

$$\mathbf{S} = \mathbf{S_o} \cdot (\mathbf{I} + \alpha_M \mathbf{N}) + \alpha_A \mathbf{N'} \tag{S13}$$

with $\mathbf{I}$, the $2N \times 2N$ identity matrix. The constants α_M and α_A are tuned such that the signal-to-noise ratio (SNR) is close to the experimental one (SNR$\sim$ 8.5 dB) and such that the respective weight of multiplicative and additive noise is the same as in experiment. Note that the results would be similar for other ratios between multiplicative and additive noise.

The matrix $\mathbf{S}$ of Eq.S13 displays the same statistical properties as the experimental one. The singular value decomposition of the transmission matrix $\mathbf{t}$ is then performed,

$$\mathbf{t} = \mathbf{u}\sqrt{\mathcal{T}}\mathbf{v}^\dagger \tag{S14}$$

$\mathbf{u}$ and $\mathbf{v}$ are unitary matrices of dimension $N \times N$ whose columns, $\mathbf{u_i}$ and $\mathbf{v_i}$, correspond to the transmission eigenchannels at the input and output, respectively. $\mathcal{T}=$ diag $(T_1, \ldots, T_N)$ is a diagonal matrix containing the N transmission eigenvalues of $\mathbf{tt}^\dagger$. Their mean distribution $\rho(T)$ is computed by averaging their histogram over the whole set of realizations of $\mathbf{S}$. The result is shown in Fig. 4(a) and compared to the expected bimodal law. As in our experiment, noise breaks the unitarity of the $\mathbf{S}-$matrix and one obtains unphysical transmission eigenvalues superior to 1. However, here, unlike in the experiment, we have access to the *true* transmission matrix $\mathbf{t_o}$. Hence, one can compute the *true* transmission coefficients, T_i', associated to the i^{th} input eigenchannel $\mathbf{u_i}$,

$$T_i' = \mathbf{u_i}^\dagger \mathbf{t_o} \mathbf{t_o}^\dagger \mathbf{u_i} \tag{S15}$$

Their mean distribution $\rho(T')$ is obtained by averaging their histogram over the whole set of realizations of $\mathbf{S}$. The result is shown in Fig. 4(b) and compared to the bimodal law. Although $\rho(T')$ still displays a bimodal lineshape, the peak corresponding to open channels is repelled around $T' \sim 0.8$. This confirms that noise in the $\mathbf{S}$-matrix prevents from addressing fully open channels. This is in agreement with the wave-field associated to the open eigenchannel deduced from the measured $\mathbf{S}-$matrix displayed in Fig. 3(c) of the accompanying letter. This channel is actually not fully transmitted across the scattering medium [see Fig. 3(g) of the accompanying letter].

We now investigate numerically the effect of the normalization of the measured $\mathbf{S}$-matrix proposed in the paper. The eigenvalues of the *noisy* scattering matrix $\mathbf{S}$ are normalized as prescribed by Eq.2 of the accompanying Letter. From the normalized scattering matrix $\hat{\mathbf{S}}$, one can extract a corrected transmission matrix $\hat{\mathbf{t}}$. Its singular value decomposition can be performed

$$\hat{\mathbf{t}} = \hat{\mathbf{u}}\sqrt{\hat{\mathcal{T}}}\hat{\mathbf{v}}^\dagger \tag{S16}$$

$\hat{\mathbf{u}}$ and $\hat{\mathbf{v}}$ are unitary matrices whose columns, $\hat{\mathbf{u}}_\mathbf{i}$ and $\hat{\mathbf{v}}_\mathbf{i}$, correspond to the transmission eigenchannels at the input and output, respectively. $\hat{\mathcal{T}}=$ diag $\left(\hat{T}_1, \ldots, \hat{T}_N\right)$ is a diagonal matrix containing the N transmission eigenvalues of $\hat{\mathbf{t}}\hat{\mathbf{t}}^\dagger$. Their mean distribution $\hat{\rho}(\hat{T})$ is computed by averaging their histogram over the whole set of realizations of $\hat{\mathbf{S}}$. $\hat{\rho}(\hat{T})$ closely follows the bimodal law [see Fig. S1(c)], as already pointed out with the normalized experimental $\hat{\mathbf{S}}-$matrix in the accompanying Letter. However, one could claim that these transmission eigenvalues have not any physical meaning and do not represent the *true* transmission coefficients as the unitarity of $\hat{\mathbf{S}}$ is forced. To refute this argument, one can compute the *true* transmission coefficient, $\hat{T}_i'$, associated to the i^{th} input eigenchannel $\hat{\mathbf{u}}_\mathbf{i}$

$$\hat{T}_i' = \hat{\mathbf{u}}_\mathbf{i}^\dagger \mathbf{t_o} \mathbf{t_o}^\dagger \hat{\mathbf{u}}_\mathbf{i} \tag{S17}$$

Their mean distribution $\hat{\rho}(\hat{T}')$ is shown in Fig. 4(d). $\hat{\rho}(\hat{T}')$ closely follows the bimodal law. The comparison with $\rho(T')$ (Fig. 4(b)) illustrates how the normalization of $\mathbf{S}$ allows to retrieve almost completely the open eigenchannels. The maximum *true* transmission coefficient is here of 97.5%. This is in agreement with the wave-field associated to the open eigenchannel deduced from the measured $\mathbf{S}-$matrix displayed in Fig. 3(d) of the accompanying letter. This channel was shown to be almost fully transmitted across the scattering medium [see Fig. 3(g) of the accompanying letter].

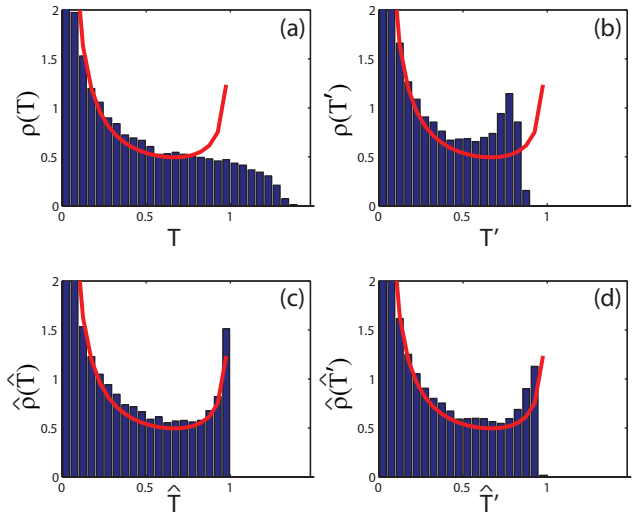

FIG. S4: Mean distributions, $\rho(T)$ (a), $\rho(T')$ (b), $\hat{\rho}(\hat{T})$ (c) and $\hat{\rho}(\hat{T}')$ (d), obtained by averaging over the whole set of numerical realizations of $\mathbf{S}$ for a SNR of 8.5 dB (analogous to the experimental SNR).

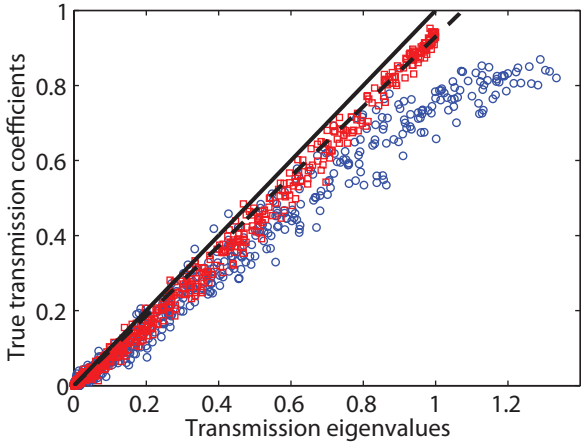

FIG. S5: True transmission coefficients, T' (blue circles) and $\hat{T}'$ (red squares), vs transmission eigenvalues, T and $\hat{T}$, respectively. The line of unity slope is shown for comparison (black continuous line). The $\hat{T}'$ vs $\hat{T}$ cloud of points are fitted with a slope of 0.93 (black dashed line).

Fig. S5 displays the true transmission coefficients T' and $\hat{T}'$ versus the transmission eigenvalues T and $\hat{T}$. Not surprisingly, the transmission eigenvalues T deduced from the *noisy* $\mathbf{S}-$matrix do not match the associated transmission coefficients T', especially for large transmission eigenvalues. Interestingly, the transmission eigenvalues $\hat{T}$ deduced from the normalized $\hat{\mathbf{S}}-$matrix are strongly correlated to the associated transmission coefficients T' since the associated cloud of points is close to the line of slope 1 in Fig. S5. This proves again the validity of the $\mathbf{S}-$matrix normalization that allows to retrieve the open eigenchannels across the disordered medium in presence of noise and obtain with a good precision the associated transmission coefficients (error of 7%).

MEASUREMENT OF THE WAVE-FIELD ASSOCIATED TO EACH EIGENCHANNEL

This section describes the experimental procedure followed to measure the wave-field associated to each eigenchannel. Impulse responses are measured between the line of sources and a grid of points that maps the scattering medium, following the same procedure used for the measurement of the $\mathbf{S}$-matrix. The grid pitch is 1 mm. The whole set of impulse responses forms a transmission matrix $\mathbf{k}(t)$. A temporal Fourier transform of $\mathbf{k}$ is performed. The wave-field associated to an incident plane wave is obtained by performing the product between the eigenvector $[1\cdots1]$ and the matrix $\mathbf{k}(f)$. For the wave-field associated to each eigenchannel, the columns of $\mathbf{k}$ are first decomposed in the channel basis. The wave-field associated to an eigenchannel corresponds to the product between the corresponding eigenvector $\mathbf{u_i}$ of $\mathbf{tt}^\dagger$ and the matrix $\mathbf{k}$.

* Electronic address: alexandre.aubry@espci.fr

[1] M. C. Cross and R. Lifshitz, Phys. Rev. B **64**, 085324 (2001).
[2] D. H. Santamore and M. C. Cross, Phys. Rev. B **66**, 144302 (2002).
[3] S. Krishnaswami, Ultrasonic Nondestructive Evaluation (CRC Press, Boca Raton, FL, 2004), chap. Theory and applications of laser-ultrasonic techniques, pp. 435–494.